IEEE Access
Multidisciplinary | Rapid Review | Open Access Journal

Received 12 August 2023, accepted 23 August 2023, date of publication 28 August 2023, date of current version 31 August 2023.

Digital Object Identifier 10.1109/ACCESS.2023.3308906

RESEARCH ARTICLE

A Full-Aperture Frequency Scaling Algorithm for Processing Dechirped Sliding Spotlight SAR Data

YOUNG-GEUN KANG AND SEONG-OOK PARK, (Senior Member, IEEE)
School of Electrical Engineering, Korea Advanced Institute of Science and Technology, Daejeon 34141, South Korea

Corresponding author: Young-Geun Kang (kbdj25@kaist.ac.kr)

This work was supported in part by the Institute of Information and Communications Technology Planning and Evaluation (IITP) Grant through the Korea Government (MSIT), Key Technologies Development for Next Generation Satellites, under Grant 2018-0-01658.

ABSTRACT This paper proposes a full-aperture method for processing sliding spotlight synthetic aperture radar (SAR) data with dechirp-on-receive. The frequency scaling algorithm (FSA) efficiently processes the dechirped signals because the range cell migration correction (RCMC) process involves removing the residual video phase. However, the conventional FSA combined with the sub-aperture method is unsuitable for processing sliding mode data because the azimuth extent of the SAR image is limited by the system pulse repetition frequency. In addition, the azimuth compression performance deteriorates as the range displacement increases from the center of the SAR image. To address these problems, we developed a modified full-aperture FSA for sliding mode data processing. A complete signal model of the azimuth convoluted sliding mode data with the dechirp-on-receive is newly derived. Based on the signal model, the frequency scaling factor and azimuth-matched filter have been modified to accurately perform RCMC and azimuth compression. Point target simulations demonstrated two advantages of the proposed algorithm over the conventional sub-aperture approach; One is accurate and consistent azimuth compression performance regardless of range displacements, and the other is wide observable azimuth extent. The practicality of the proposed method is further verified through actual SAR raw data experiments. In addition, it is analyzed that the proposed algorithm is specialized in processing dechirped sliding mode data through a characteristic comparison with various traditional sliding spotlight processing methods.

INDEX TERMS Azimuth convolution, dechirp-on-receive, frequency scaling algorithm, full-aperture method, sliding spotlight mode, synthetic aperture radar.

I. INTRODUCTION

Synthetic aperture radar (SAR) is an imaging radar that acquires a two-dimensional image over the observed area. Sliding spotlight mode is a good compromise between the strip-map mode [1], [2] and the staring spotlight mode [3], [4], generating high azimuth resolution images over a wide azimuth extent. In the sliding mode [4], [9], [10], [11], the azimuth width is extended by sliding the antenna beam illuminated area in the flight (azimuth) direction. This feature produces SAR images with a higher azimuth resolution than the strip-map mode and a wider azimuth extent than the staring mode. Due to these properties, the sliding mode is widely used as one of the main operating modes of modern SAR satellites, such as TerraSAR-X and Gaofen-3 [26], [27], [28], [29]. Accordingly, extensive research has been conducted on the processing of sliding mode SAR data [20], [21], [22], [23], [24], [25], [26], [27], [28], [29], [30], [31], [32], [33], [34], [35], [36].

It is necessary to employ wide-bandwidth chirp signals to achieve a range resolution as high as the azimuth resolution in the spotlight mode. A high sampling rate receiver with large-capacity storage is required to process the wide-bandwidth chirp signals without aliasing. The dechirp-on-receive technique alleviates these high-performance hardware requirements by reducing the bandwidth of the received signal [3], [4], [5], [6], [7], [8]. Therefore, obtaining the sliding mode data through the dechirp-on-receive method results

The associate editor coordinating the review of this manuscript and approving it for publication was Chengpeng Hao.

in data capable of efficiently generating high-resolution SAR images. Nevertheless, because studies on the algorithm for the corresponding data are insufficient, we researched a method for processing the signal model of the dechirped sliding mode data.

A novel frequency scaling algorithm (FSA) has been proposed to process the dechirped staring mode data [19]. The FSA efficiently processes the dechirped signal because the frequency scaling process that performs the range cell migration correction (RCMC) includes the residual video phase (RVP) removal. The FSA in [19] is incorporated with the sub-aperture technique, an efficient method of processing synthetic aperture data by dividing it into sub-apertures [12], [13], [14], [15], [16]. The sub-aperture methods are widely used for SAR data processing because the pulse repetition frequency (PRF) of the SAR system only needs to cover the instantaneous bandwidth corresponding to each sub-aperture [12], [13], [14], [15], [16], [17], [18], [19], [20], [21], [22], [23], [24], [25], [26]. On the other hand, sub-aperture processing has a drawback in that the azimuth compression performance is sensitive to the accuracy of the estimated effective velocity for each sub-aperture. The number and length of sub-apertures also affect the algorithm performance [21], [35].

Several methods without sub-aperture techniques have been proposed to address the shortcomings of sub-aperture processing [35], [36], [37]. In [37], a two-step focusing method for processing spotlight mode data is introduced, which first implements azimuth convolution to resolve the back-folded Doppler bandwidth and then focuses residual data via the strip-map processing technique. However, because the method is designed for staring mode data processing, frequency aliasing may occur when applied to sliding mode data [35]. In [35], an extended three-step focusing algorithm has been proposed to process the sliding mode data. However, a chirped signal model is selected as the target signal, and accordingly, the chirp scaling algorithm (CSA) has been adopted as the processing scheme. This implies that the method is not suitable for processing dechirped data because the CSA is inefficient for the signal model due to its high requirements on the range sampling rate and azimuth filter length [19]. In [36], a generalized three-step focusing scheme incorporated with a modified range migration algorithm has been proposed for processing squinted sliding mode data. However, the method is also designed for chirped signals, making it incompatible with the dechirped signal model.

As such, although many studies on the full-aperture processing for sliding mode SAR data are being actively conducted [27], [28], [29], [30], [31], [32], [33], [34], [35], [36], most of the studies on full-aperture processing performed so far are based on algorithms that do not consider the dechirped signal model [27], [28], [29], [30], [31], [32], [33], [34], [35], [36], [37], [38], [39], [40], [41], [42], [43], [44]. As mentioned above, FSA is a method that efficiently processes the dechirped signal model. However, the conventional FSA combined with the sub-aperture approach is unsuitable for processing sliding mode data with a wide azimuth swath. This is because the azimuth image domain of the sub-aperture FSA is a frequency domain, and therefore the azimuth extent is limited by the system PRF value. In addition, azimuth compression performance is degraded in areas where the range displacements from the center of the SAR image are significant. Therefore, we developed a full-aperture FSA method for processing the dechirped sliding mode data to address the problems above.

In the proposed full-aperture method, because an azimuth convolution process is preceded before applying the FSA, a complete two-dimensional signal model of azimuth convoluted sliding spotlight data with the dechirp-on-receive is newly derived in the range-Doppler domain. Based on the derived signal model, the FSA is modified for sliding mode and full-aperture method. A newly designed frequency scaling factor and an azimuth-matched filter are introduced to perform RCMC and azimuth compression, respectively.

This paper is organized as follows. Section II briefly reviews the data acquisition geometry and signal model of the dechirped sliding mode data. And also, a space-wavenumber diagram (SWD) of the azimuth signal and the total Doppler bandwidth in the wavenumber domain are presented. The detailed derivation process for the signal model of the azimuth convoluted sliding mode data with the dechirp-on-receive in the range-Doppler domain and the proposed algorithm are given in Section III. In Section IV, point target simulations and actual SAR raw data processing results are presented and compared with the conventional sub-aperture FSA. A comparison between the proposed and various traditional sliding spotlight processing methods based on the aperture approach and compatible signal models is also given. Finally, the conclusion is given in Section V.

II. DATA ACQUISITION GEOMETRY AND DECHIRPED SIGNAL MODEL OF SLIDING SAR DATA

This Section reviews the data acquisition geometry and the dechirped signal model of the sliding SAR data. Note that the signal models in this paper are represented in the space-wavenumber domain rather than the time-frequency domain for the concise expression of the equations. The SWD will be continuously updated in Section III to demonstrate the effects of each step of the proposed method.

The stereoscopic data acquisition geometry of the sliding mode is illustrated in Fig. 1(a). x is the azimuth spatial location of the SAR platform, r is the slant range, X_{tot} is the total synthetic aperture length, v_r is the effective velocity of the SAR platform, v_b is the antenna beam footprint velocity, k_s is the beam steering angular wavenumber, H is the SAR platform height, r_c is the distance between the radar straight track and the center of the imaging area, and r_{rot} is the distance between the radar straight track and the antenna beam rotation center. To visually show the synthetic aperture length of a point target in sliding mode, a simplified planar data acquisition geometry is added in Fig. 1(b). X_{sm} is the synthetic aperture length of a point target in strip-map mode,

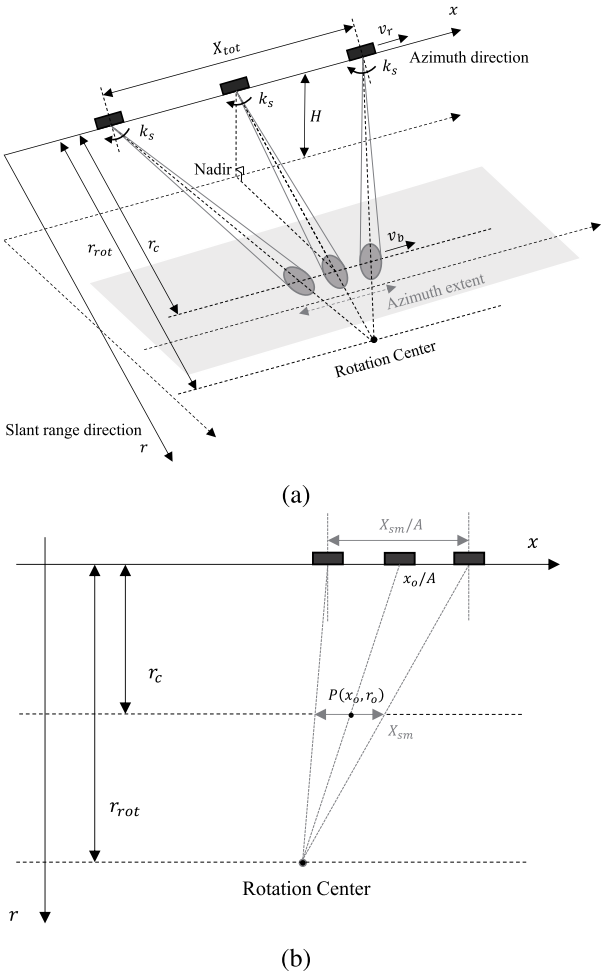

FIGURE 1. (a) A stereoscopic data acquisition geometry of sliding mode, (b) a planar data acquisition geometry to derive the azimuth envelope function of a point target in sliding mode.

x_o is the azimuth spatial location of a point target, r_o is the range of the closest approach of the target, and $A = v_b/v_r$ is the sliding factor [40]. From the geometry, a signal model of the received and down-converted sliding SAR data with the dechirp-on-receive for the point target $P(x_o, r_o)$ is obtained as follows:

$$\begin{aligned} s(x,r) = C \cdot \mathrm{rect}\left[\frac{Ax - x_o}{X_{sm}}\right] \cdot \exp[-j2k \cdot r(x)] \\ \times \mathrm{rect}\left[\frac{r - r(x)}{R}\right] \cdot \exp[j2b \cdot (r(x) - r_c) \cdot (r - r_c)] \\ \times \exp[-jb \cdot (r(x) - r_c)^2] \end{aligned} \tag{1}$$

where C is the constant with varying amplitude and constant phase, rect[·] is the rectangular function, k is the wavenumber, $r(x)$ is the distance between the radar and the target according to x, R is the pulse range extent, and b is the pulse frequency (wavenumber) modulation rate. Note that constant terms that are negligible in the signal analysis will be omitted in the subsequent formulas for brevity. The first rectangular function represents the azimuth envelope function of the point

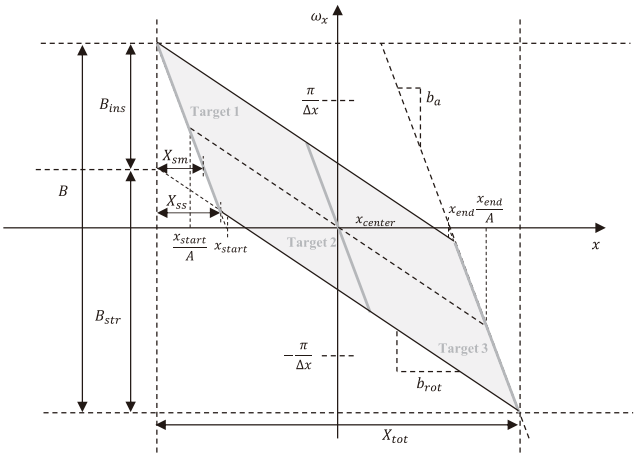

FIGURE 2. Azimuth SWD of sliding mode SAR signal. Three fully observed targets are indicated by gray-bold lines.

target in the sliding mode and is derived from Fig. 1(b). The first exponential term describes the azimuth modulation of the signal. The second exponential term represents the range signal, and the last means the RVP. In small squint cases, $r(x)$ can be approximated as the following equation [1].

$$r(x) \approx r_o + \frac{(x - x_o)^2}{2r_o} \tag{2}$$

By substituting (2) into (1), the azimuth component of the signal model is rewritten as follows:

$$s_a(x) = \mathrm{rect}\left[\frac{Ax - x_o}{X_{sm}}\right] \cdot \exp\left[j\frac{1}{2} \cdot b_a \cdot (x - x_o)^2\right] \tag{3}$$

where $b_a = -2k/r_o$ is the Doppler rate in the wavenumber domain. Fig. 2 shows the azimuth SWD of the sliding mode derived from the azimuth component of the signal model. x_{center} is the azimuth spatial location of an object positioned at the center of the azimuth extent so that the target is broadside the SAR platform at $x = 0$. x_{start} and x_{end} are the azimuth spatial locations of the fully observed targets on the leftmost and rightmost sides of the azimuth extent, respectively. The Δx is the azimuth spatial interval between adjacent SAR system pulses and the ω_x is the azimuth wavenumber. Note that the synthetic aperture lengths of targets are extended to $X_{ss} = X_{sm}/A$ in the sliding mode because of the antenna beam steering. In the spotlight mode, the Doppler centroid has a space-varying characteristic because the antenna beam rotates with the beam steering angular wavenumber k_s. This characteristic makes the total Doppler bandwidth of the signal wider. The varying rate of the Doppler centroid is equal to the Doppler rate in the staring mode, whereas, it is defined as follows according to r_{rot} in the sliding mode.

$$b_{rot} = -\frac{2k}{r_{rot}} \tag{4}$$

The Doppler wavenumber of each target and the Doppler centroid decrease with the rates b_a and b_{rot}, respectively,

according to the azimuth space, as shown in Fig. 2. Accordingly, the total bandwidth is greater than the system pulse repetition wavenumber $2\pi/\Delta x$. The total Doppler bandwidth B in the wavenumber domain is as follows:

$$B = B_{ins} + B_{str} = |b_a|X_{sm} + |b_{rot}|X_{tot} \tag{5}$$

where B_{ins} is the Doppler instantaneous bandwidth caused by the azimuth antenna beamwidth, and B_{str} is the Doppler bandwidth caused by the antenna beam steering. Though the additional Doppler bandwidth due to the squint angle also exists [47], it is negligible in small squint cases. The widened Doppler bandwidth over the pulse repetition wavenumber of the SAR system introduces aliasing, making SAR processing difficult.

III. PROPOSED FULL-APERTURE FREQUENCY SCALING ALGORITHM FOR DECHIRPED SLIDING MODE DATA

The complete block diagram of the proposed full-aperture method is given in Fig. 3. The processing steps consist of preliminary azimuth convolution, FSA modified for sliding mode and full-aperture processing, and post azimuth convolution. First, to deal with the wide Doppler bandwidth of the sliding mode data, an azimuth convolution process in the space domain is preceded before performing the FSA. Convolution with the selected chirp signal to avoid aliasing is a widely used technique in full-aperture spotlight SAR processing [27], [28], [29], [30], [31], [35], [36], [37], [38], [39]. A new signal model is derived after the preliminary azimuth convolution since the dechirped signal model is addressed in this paper. Next, based on the derived signal model, a new scaling factor and modified azimuth-matched filter are introduced to accurately perform RCMC and azimuth compression. Because the azimuth extent is compressed by the preliminary azimuth convolution, the SAR image immediately after the FSA may be aliased. Therefore, the algorithm is incorporated with the post azimuth convolution in the wavenumber domain after the FSA to avoid aliasing in the SAR image domain (space domain).

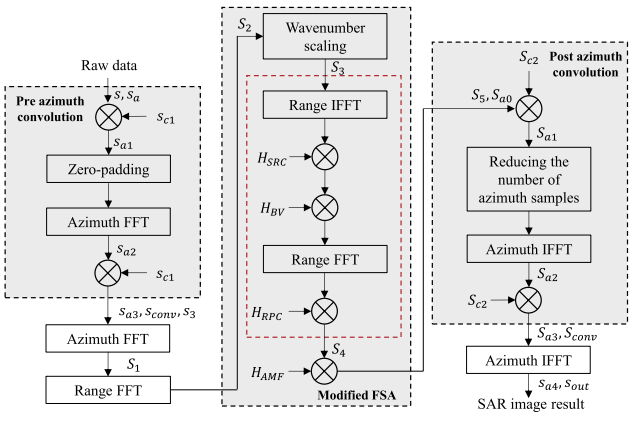

FIGURE 3. Block diagram of the proposed full-aperture FSA method for dechirped sliding mode data.

A. PRELIMINARY AZIMUTH CONVOLUTION

In the preliminary azimuth convolution step, only the azimuth component of the signal model is considered for simplicity. As shown in Fig. 2, the total Doppler bandwidth of the signal is greater than the SAR system pulse repetition wavenumber due to the antenna beam steering. The azimuth convolution incorporated with zero-padding intentionally extends the pulse repetition wavenumber to include the entire Doppler bandwidth in the baseband. It has been proven that convolution with a chirp signal of the rate $-b_{rot}/2$ produces a minimum output azimuth extent signal in the sliding mode [35], [36]. Minimum output azimuth extent is the most efficient case as it requires the fewest number of zero-padding afterward. Therefore, the selected chirp signal and the result of the convolution are as follows, respectively.

$$s_{c1}(x) = \exp\left[-j\frac{1}{2}\cdot b_{rot}\cdot x^2\right] \tag{6}$$

$$\begin{aligned} s_{conv}(x) &= s_a(x) * s_{c1}(x) \\ &= s_{c1}(x)\cdot\int\left(s_a(x')\cdot s_{c1}(x')\right)\cdot\exp[jb_{rot}xx']dx' \end{aligned} \tag{7}$$

In (7), $*$ is the azimuth convolution operator. The big parenthesis term in the integral sign is the first multiplication step in the preliminary azimuth convolution in Fig. 3. The result of multiplying (3) and (6) is as follows.

$$\begin{aligned} s_{a1}(x) = \text{rect}\left[\frac{Ax - x_o}{X_{sm}}\right] \\ \times \exp\left[-jb_a x_o x + j\frac{1}{2}\cdot(b_a - b_{rot})\cdot x^2\right] \end{aligned} \tag{8}$$

The next step is to implement the integral in (7), which is very tedious and complicated. But fortunately, it has been proven that the integration process can be replaced by Fourier transform (FFT) if the number of azimuth pixels is adjusted through zero-padding to satisfy a specific condition [36]. The condition is as follows:

$$N_1 = -\frac{2\pi}{\Delta x\cdot\Delta x_{zp}\cdot b_{rot}} \tag{9}$$

where N_1 is the adjusted number of azimuth pixels, and Δx_{zp} is the intentionally narrowed azimuth spatial interval between pulses after zero-padding. A minus sign is added because b_{rot} is a negative value. To prevent Doppler aliasing by allowing the entire Doppler band to exist within the baseband, Δx_{zp} must satisfy the following condition.

$$\Delta x_{zp} \le \frac{2\pi}{B} \tag{10}$$

Therefore, N_1 is determined by determining the Δx_{zp} value that satisfies condition (10) and substituting it into (9). Now that the integration process is replaced by FFT, the following equation is obtained by implementing the azimuth FFT using

the principle of stationary phase (POSP) technique [45].

$$s_{a2}(x) = \mathrm{rect}\left[\frac{(A-1)\cdot x}{X_{sm}}\right] \times \exp\left[-j\frac{1}{2}\cdot\frac{1}{b_a - b_{rot}}\cdot(b_{rot}x - b_a x_o)^2\right] \tag{11}$$

The final step of the preliminary azimuth convolution is to perform the multiplication before the integral sign in (7). Multiplying (11) by $s_{c1}(x)$, the following equation is obtained:

$$s_{a3}(x) = \mathrm{rect}\left[\frac{(A-1)\cdot x}{X_{sm}}\right]\cdot\exp\left[-j\frac{1}{2}\cdot b_m\cdot(x-x_o)^2\right] \tag{12}$$

where b_m is the modified Doppler rate through the azimuth convolution, which is defined as follows.

$$b_m = \frac{b_a\cdot b_{rot}}{b_a - b_{rot}} \tag{13}$$

As shown in the exponential term in (12), the Doppler rate of all targets in the image swath is unified as $-b_m$ regardless of their azimuth spatial locations. And also, as shown in the rectangular function in (12), the azimuth extent of all targets is unified as $X_{sm}/(1-A)$ at $x = 0$ regardless of their azimuth spatial locations. The first rectangular function in (27), which is the azimuth transformed signal of (12), means that the Doppler bandwidth of the target is formed as wide as B_{ins}/A at $\omega_x = b_m x_o$ in the Doppler wavenumber domain. The derivation process of (27) is given in Section II-B. The azimuth SWD after the preliminary azimuth convolution derived from the above facts is shown in Fig. 4. It is confirmed that the aliased Doppler spectrum is resolved because the pulse repetition wavenumber is extended through the azimuth convolution so that the total Doppler bandwidth exists in the baseband. Note that the processing azimuth extent is compressed as $X_1 = N_1\cdot\Delta x_{zp} = X_{sm}/(1-A)$.

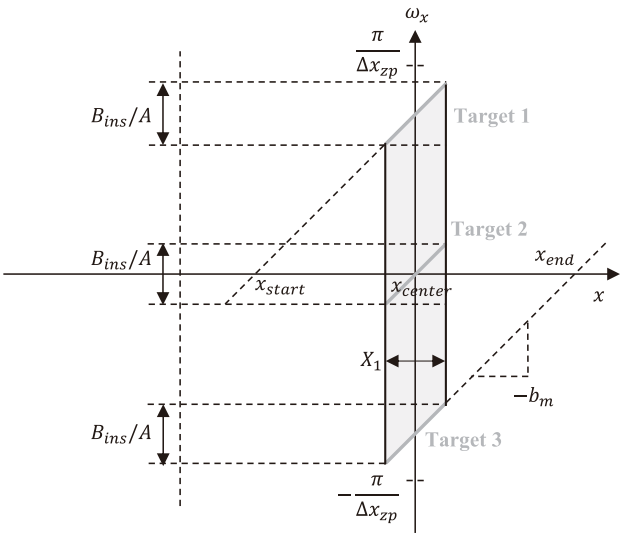

FIGURE 4. Azimuth SWD of sliding mode SAR signal after the preliminary azimuth convolution process.

B. MODIFIED FREQUENCY SCALING ALGORITHM FOR SLIDING MODE AND FULL-APERTURE PROCESSING

The signal terms unrelated to the azimuth convolution were omitted in the preliminary azimuth convolution stage. However, these terms should not be omitted further because the subsequent process cause significant changes to these terms. (12) is rewritten as follows in consideration of the complete two-dimensional signal model.

$$s_3(x,r) = \mathrm{rect}\left[\frac{(A-1)\cdot x}{X_{sm}}\right]\cdot\exp\left[-j\frac{1}{2}\cdot b_m\cdot(x-x_o)^2\right] \times \mathrm{rect}\left[\frac{r-r(x)}{R}\right]\cdot\exp[j2b\cdot(r(x)-r_c)\cdot(r-r_c)] \times \exp[-jb\cdot(r(x)-r_c)^2] \tag{14}$$

From (14), we newly derived an azimuth convoluted range-Doppler signal model of the dechirped sliding mode data. The derivation process consists of the following three main steps: 1) Range Fourier transform, 2) Range inverse Fourier transform, and 3) Azimuth Fourier transform.

1) RANGE FOURIER TRANSFORM

To perform range FFT, (14) is rewritten as follows by arranging the terms related to the slant range r.

$$\begin{aligned} &s_0(x,r) \\ &= \mathrm{rect}\left[\frac{(A-1)\cdot x}{X_{sm}}\right]\cdot\exp\left[-j\frac{1}{2}\cdot b_m\cdot(x-x_o)^2\right] \\ &\quad\times\exp[-j2b\cdot(r(x)-r_c)\cdot r_c]\cdot\exp[-jb\cdot(r(x)-r_c)^2] \\ &\quad\times\mathrm{rect}\left[\frac{r-r(x)}{R}\right]\cdot\exp[j2b\cdot(r(x)-r_c)\cdot r] \end{aligned} \tag{15}$$

The terms in the bottom row in Eq. (15) are terms related to the slant range r. Therefore, the range FFT result is as follows:

$$\begin{aligned} &S_0(x,\omega_r) \\ &= \mathrm{rect}\left[\frac{(A-1)\cdot x}{X_{sm}}\right]\cdot\exp\left[-j\frac{1}{2}\cdot b_m\cdot(x-x_o)^2\right] \\ &\quad\times\exp[-j2b\cdot(r(x)-r_c)\cdot r_c]\cdot\exp[-jb\cdot(r(x)-r_c)^2] \\ &\quad\times\mathrm{sinc}\left[\frac{R}{2}\cdot(\omega_r - 2b\cdot(r(x)-r_c))\right] \\ &\quad\times\exp[-jr(x)\cdot(\omega_r - 2b\cdot(r(x)-r_c))] \end{aligned} \tag{16}$$

where ω_r is the range wavenumber.

2) RANGE INVERSE FOURIER TRANSFORM

(16) is rewritten by arranging the terms related to the range wavenumber ω_r and introducing two chirp signals to generate

the RVP term to be convoluted later.

$$\begin{aligned} & S_0(x,\omega_r) \\ &= \mathrm{rect}\left[\frac{(A-1)\cdot x}{X_{sm}}\right]\cdot\exp\left[-j\frac{1}{2}\cdot b_m\cdot(x-x_o)^2\right] \\ &\quad\times\exp[jb\cdot(r(x)-r_c)^2] \\ &\quad\times\mathrm{sinc}\left[\frac{R}{2}\cdot(\omega_r-2b\cdot(r(x)-r_c))\right] \\ &\quad\times\exp[-jr(x)\cdot\omega_r]\cdot\exp\left[j\frac{\omega_r^2}{4b}\right]\cdot\exp\left[-\frac{\omega_r^2}{4b}\right] \end{aligned} \tag{17}$$

The signal convoluted with the RVP term is a useful model as it is advantageous for subsequent wavenumber scaling. The terms in the bottom two rows in (17) are terms related to the range wavenumber ω_r. The range inverse Fourier transform (IFFT) result is as follows.

$$\begin{aligned} & s_0(x,r) \\ &= \mathrm{IFFT}_r\left\{\mathrm{rect}\left[\frac{(A-1)\cdot x}{X_{sm}}\right]\cdot\exp[jb\cdot(r(x)-r_c)^2]\right. \\ &\quad\times\exp\left[-j\frac{1}{2}\cdot b_m\cdot(x-x_o)^2\right] \\ &\quad\times\mathrm{sinc}\left[\frac{R}{2}\cdot(\omega_r-2b\cdot(r(x)-r_c))\right] \\ &\quad\left.\times\exp[-jr(x)\cdot\omega_r]\cdot\exp\left[j\frac{\omega_r^2}{4b}\right]\right\}*\exp[jbr^2] \end{aligned} \tag{18}$$

By defining a new variable as $\Omega=\omega_r-2b\cdot(r(x)-r_c)$ and substituting it into (18), the following equation is obtained.

$$\begin{aligned} & s_0(x,r) \\ &= \left\{\mathrm{rect}\left[\frac{(A-1)\cdot x}{X_{sm}}\right]\cdot\exp\left[-j\frac{1}{2}\cdot b_m\cdot(x-x_o)^2\right]\right. \\ &\quad\times\exp[-j2b\cdot(r(x)-r_c)\cdot r_c]\cdot\mathrm{IFFT}_r\left\{\mathrm{sinc}\left[\frac{R}{2}\Omega\right]\right. \\ &\quad\left.\left.\times\exp\left[j\frac{\Omega^2}{4b}\right]\cdot\exp[-jr_c\Omega]\right\}\right\}*\exp[jbr^2] \end{aligned} \tag{19}$$

The IFFT_r term in (19) is:

$$\begin{aligned} & \mathrm{IFFT}_r\left\{\mathrm{sinc}\left[\frac{R}{2}\Omega\right]\cdot\exp\left[j\frac{\Omega^2}{4b}\right]\cdot\exp[-jr_c\Omega]\right\} \\ &= \exp[j2b\cdot(r(x)-r_c)\cdot r]\cdot\int\mathrm{sinc}\left[\frac{R}{2}\Omega\right] \\ &\quad\times\exp\left[j\frac{\Omega^2}{4b}\right]\cdot\exp[j\Omega\cdot(r-r_c)]d\Omega \\ &= \mathrm{rect}\left[\frac{r-r_c}{R}\right]\cdot\exp[j2b\cdot(r(x)-r_c)\cdot r] \end{aligned} \tag{20}$$

The first exponential term in the integral is considered as 1 because $\Omega^2/4b\approx 0$ where the integral has a considerable magnitude. By substituting the formula (20) into (19), the following result is obtained.

$$\begin{aligned} s_0(x,r) &= \left\{\mathrm{rect}\left[\frac{(A-1)\cdot x}{X_{sm}}\right]\cdot\exp\left[-j\frac{1}{2}\cdot b_m\cdot(x-x_o)^2\right]\right. \\ &\quad\times\mathrm{rect}\left[\frac{r-r_c}{R}\right]\cdot\exp[j2b\cdot(r(x)-r_c)\cdot(r-r_c)]\Big\} \\ &\quad*\exp[jbr^2] \end{aligned} \tag{21}$$

Using the well-known parabolic approximation of the range equation for small squint cases given in (2) before performing the final azimuth FFT, (21) is rewritten as follows.

$$\begin{aligned} & s_0(x,r) \\ &= \left\{\mathrm{rect}\left[\frac{r-r_c}{R}\right]\cdot\exp[-j2b\cdot(r-r_c)\cdot r_c]\right. \\ &\quad\times\exp[j2b\cdot(r-r_c)\cdot r_o]\cdot\mathrm{rect}\left[\frac{(A-1)\cdot x}{X_{sm}}\right] \\ &\quad\left.\times\exp\left[j\left\{\frac{b}{r_o}\cdot(r-r_c)-\frac{b_m}{2}\right\}\cdot(x-x_o)^2\right]\right\}*\exp[jbr^2] \end{aligned} \tag{22}$$

3) AZIMUTH FOURIER TRANSFORM

By performing azimuth FFT using the POSP technique on (22), the signal model in the range-Doppler domain is obtained as follows:

$$\begin{aligned} S_0(\omega_x,r) &= \left\{\mathrm{rect}\left[\frac{r-r_c}{R}\right]\cdot\exp[-j2b\cdot(r-r_c)\cdot r_c]\right. \\ &\quad\times\exp[j2b\cdot(r-r_c)\cdot r_o]\cdot\mathrm{rect}\left[-\frac{\omega_x-b_mx_o}{B_{ins}/A}\right] \\ &\quad\times\exp\left[j\frac{1}{2b_m}\cdot\left\{1-\frac{2b}{r_ob_m}\cdot(r-r_c)\right\}^{-1}\cdot\omega_x^2\right] \\ &\quad\left.\times\exp[-j\omega_xx_o]\right\}*\exp[jbr^2] \end{aligned} \tag{23}$$

It is notable that the following approximation is applied when obtaining the azimuth envelope function because the value is much smaller than $b_m/2$.

$$\frac{b}{r_o}\cdot(r-r_c)\approx 0 \tag{24}$$

To derive a useful signal model for applying subsequent wavenumber scaling, specifically selected two conjugate signals are introduced as follows.

$$\begin{aligned} S_0(\omega_x,r) &= \left\{\mathrm{rect}\left[\frac{r-r_c}{R}\right]\cdot\exp[-j2b\cdot(r-r_c)\cdot r_c]\right. \\ &\quad\times\exp[j2b\cdot(r-r_c)\cdot r_o]\cdot\mathrm{rect}\left[-\frac{\omega_x-b_mx_o}{B_{ins}/A}\right] \\ &\quad\times\exp[jb_mr_o^2]\cdot\exp[-jb_mr_o^2] \\ &\quad\times\exp\left[j\frac{1}{2b_m}\cdot\left\{1-\frac{2b}{r_ob_m}\cdot(r-r_c)\right\}^{-1}\cdot\omega_x^2\right] \\ &\quad\left.\times\exp[-j\omega_xx_o]\right\}*\exp[jbr^2] \end{aligned} \tag{25}$$

By combining the second, fourth, and fifth exponential terms in (25), the signal model can be rewritten as the following concise expression.

$$\begin{aligned} &S_0(\omega_x, r) \\ &= \left\{ \mathrm{rect}\left[-\frac{\omega_x - b_m x_o}{B_{ins}/A} \right] \cdot \exp[-j\omega_x x_o] \right. \\ &\quad \times \exp[jb_m r_o^2] \cdot \mathrm{rect}\left[\frac{r - r_c}{R} \right] \cdot \exp[-j2b \cdot (r - r_c) \cdot r_c] \\ &\quad \left. \times \exp\left[-jb_m r_o^2 \cdot \sqrt{\left(1 - \frac{2b}{r_o b_m} \cdot (r - r_c)\right)^2 - \frac{\omega_x^2}{b_m^2 r_o^2}} \right] \right\} \\ &\quad * \exp[jbr^2] \end{aligned} \tag{26}$$

By approximating the square root term to the third-order term using the Taylor series [45], a complete range-Doppler signal model of the azimuth pre-processed sliding mode data with the dechirp-on-receive with a new scaling factor (28) is finally obtained as follows:

$$\begin{aligned} S_1(\omega_x, r) = &\mathrm{rect}\left[-\frac{\omega_x - b_m x_o}{B_{ins}/A} \right] \cdot \exp[jb_m r_o^2 \cdot (1 - \beta)] \\ &\times \exp[-j\omega_x x_o] \cdot \left\{ \mathrm{rect}\left[\frac{r - r_c}{R} \right] \cdot \mathrm{src}(\omega_x, r - r_c) \right. \\ &\left. \times \exp\left[j2b \cdot \left(\frac{r_o}{\beta} - r_c \right) \cdot (r - r_c) \right] \right\} * \exp[jbr^2] \end{aligned} \tag{27}$$

$$\beta(\omega_x) = \sqrt{1 - \frac{\omega_x^2}{b_m^2 r_o^2}} \tag{28}$$

where the src term is the secondary range compression term.

$$\begin{aligned} &\mathrm{src}(\omega_x, r) \\ &= \exp\left[-j\frac{2b^2}{b_m} \cdot \frac{\beta^2 - 1}{\beta^3} \cdot r^2 - j\frac{4b^3}{r_o b_m^2} \cdot \frac{\beta^2 - 1}{\beta^5} \cdot r^3 \right] \end{aligned} \tag{29}$$

The proposed range-Doppler signal model has two similarities and differences compared to the conventional signal model for sub-aperture processing [19]. One similarity is that the signal is convoluted with the RVP term, and the other is that the β affects the range cell migration since the range signal depends on β, which depends on the azimuth wavenumber. These similarities are useful because they indicate that the proposed signal model is also suitable for applying frequency (wavenumber) scaling, an efficient RCMC technique. On the other hand, one difference is that the scaling factor β is modified as (28), and the other is that the azimuth modulation of the signal is altered as indicated by the first exponential term in (27). It is notable that the scaling factor depends on b_m. This means that the scaling factor is modified for the sliding mode and full-aperture method since b_m depends on b_{rot} and is derived through the preliminary azimuth convolution process. It is also notable that β also depends on the range position of the target r_o. This unique property enhances the compression performance by enabling accurate RCMC over a wide range extent. Meanwhile, since the azimuth modulation of the signal has been modified, an appropriate azimuth-matched filter needs to be introduced accordingly.

A technique of performing time scaling on a function by applying four chirp functions has been proposed [46]. A frequency scaling operation has been derived from the time scaling technique and has been used to implement RCMC on the dechirped data [19]. We adopted this scaling operation in the wavenumber domain. The block diagram of the wavenumber scaling operation is shown in Fig. 5. The operation consists of a combination of multiplications with four chirp functions and four Fourier transforms. Analyzing the signal model in the two-dimensional wavenumber domain reveals why the scaling operation is advantageous for processing the dechirped data. In order to present the signal model in the two-dimensional wavenumber domain, the range FFT is performed on (27) and the result is as follows:

$$\begin{aligned} &S_2(\omega_x, \omega_r) \\ &= \mathrm{rect}\left[-\frac{\omega_x - b_m x_o}{B_{ins}/A} \right] \cdot \exp[jb_m r_o^2 \cdot (1 - \beta)] \\ &\quad \times \exp[-j\omega_x x_o] \cdot \left\{ \left[\mathrm{sinc}\left[\frac{R}{2} \cdot \left(\omega_r - 2b \cdot \left(\frac{r_o}{\beta} - r_c \right) \right) \right] \right. \right. \\ &\quad \left. \left. \times \exp[-j\omega_r r_c] \right] * \mathrm{SRC}(\omega_x, \omega_r) \right\} \cdot \exp\left[-j\frac{\omega_r^2}{4b} \right] \end{aligned} \tag{30}$$

where the SRC term is the secondary range compression term in the two-dimensional wavenumber domain. It is notable that the RVP term in (30) is similar to the first chirp function in Fig. 5. Therefore, by setting the independent variable $a = b$, the RVP term can be regarded as the first chirp function in the wavenumber scaling operation, and the (30) excluding the RVP term can be regarded as the input signal of the scaling operation. Then, the output signal of the wavenumber scaling is obtained as follows by setting the other independent variable $d = \beta$.

$$\begin{aligned} &S_3(\omega_x, \omega_r/\beta) \\ &= \mathrm{rect}\left[-\frac{\omega_x - b_m x_o}{B_{ins}/A} \right] \cdot \exp[jb_m r_o^2 \cdot (1 - \beta)] \\ &\quad \times \exp[-j\omega_x x_o] \cdot \left\{ \left[\mathrm{sinc}\left[\frac{R}{2\beta} \cdot (\omega_r - 2b \cdot (r_o - r_c \cdot \beta)) \right] \right. \right. \\ &\quad \left. \left. \times \exp\left[-j\frac{\omega_r}{\beta} r_c \right] \right] * \mathrm{SRC}\left(\omega_x, \frac{\omega_r}{\beta} \right) \right\} \end{aligned} \tag{31}$$

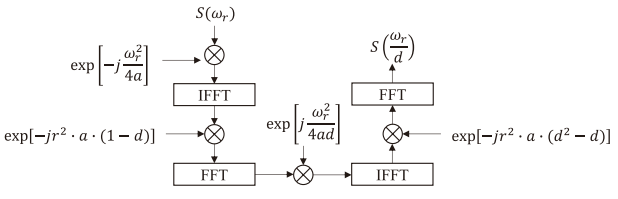

FIGURE 5. Block diagram of wavenumber scaling operation. *a* and *d* are independent variables.

As shown in (31), the RVP term has been eliminated and the range wavenumber with the peak value is now determined by the difference between r_o and $r_c \cdot \beta$. Adopting the wavenumber scaling operation to dechirped data is advantageous because the RVP term is removed accurately while performing the RCMC process. The subsequent RCMC processes are omitted in this paper because the process is similar to the conventional FSA [19]. The omitted processes are represented by the red dashed box in Fig. 3. The RCMC completed signal is as follows.

$$\begin{aligned} &S_4(\omega_x, \omega_r) \\ &= \mathrm{rect}\left[-\frac{\omega_x - b_m x_o}{B_{ins}/A} \right] \cdot \exp[jb_m r_o^2 \cdot (1-\beta)] \\ &\quad \times \exp[-j\omega_x x_o] \cdot \mathrm{sinc}\left[\frac{R}{2\beta} \cdot \left(\omega_r - 2b \cdot (r_o - r_c) \right) \right] \end{aligned} \tag{32}$$

In (32), the range wavenumber representing the range position of the point target is now only related to the distance between the point target and the scene center. The first exponential term in (32) is the azimuth modulation of the signal. This term needs to be removed to perform the azimuth compression. It is simply removed by multiplying the conjugate term of it, therefore, the modified azimuth-matched filter and the result of the matched filtering are as follows, respectively.

$$H_{AMF}(\omega_x) = \exp[-jb_m r_o^2 \cdot (1-\beta)] \tag{33}$$

$$\begin{aligned} S_5(\omega_x, \omega_r) &= \mathrm{rect}\left[-\frac{\omega_x - b_m x_o}{B_{ins}/A} \right] \cdot \exp[-j\omega_x x_o] \\ &\quad \times \mathrm{sinc}\left[\frac{R}{2\beta} \cdot \left(\omega_r - 2b \cdot (r_o - r_c) \right) \right] \end{aligned} \tag{34}$$

Since the azimuth chirp signal is removed, azimuth compression will be completed only by performing azimuth IFFT, which is very simple compared to the azimuth compression step of conventional FSA. However, if the azimuth compression is performed immediately after the modified FSA, high-quality SAR images are not obtainable. The reasons are shown in the azimuth compressed signal (35) and the azimuth SWD at this stage (Fig. 6).

$$s_{a0}(x) = \mathrm{sinc}\left[\frac{1}{2} \cdot \frac{B_{ins}}{A} \cdot (x - x_o) \right] \cdot \exp[jb_m x_o x] \tag{35}$$

As shown in (35), because the phase term is dependent on the azimuth spatial location of the target, a phase difference occurs according to the azimuth spatial location of the target. In addition, since the processing azimuth extent was compressed to X_1 due to the preliminary azimuth convolution, if X_1 does not include x_{start} and x_{end} (in most cases except for the case where the total synthetic aperture length is very short), aliasing occurs in the space domain when the azimuth IFFT is performed at this stage. Therefore, the post azimuth convolution process is followed.

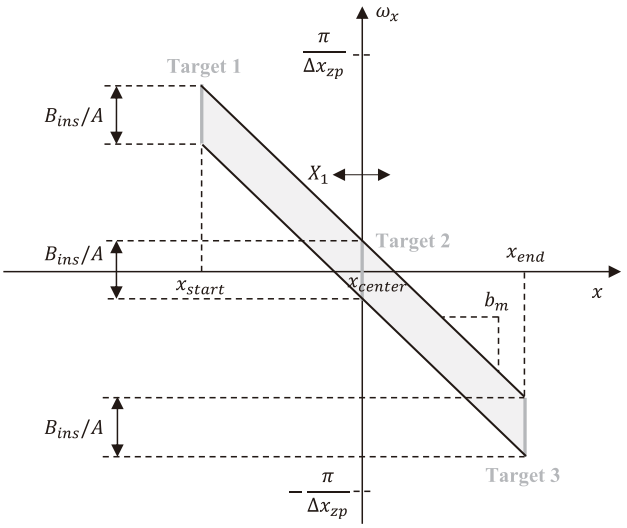

FIGURE 6. Azimuth SWD of sliding mode SAR signal after the modified FSA process.

C. POST AZIMUTH CONVOLUTION

As azimuth convolution was performed in the space domain to resolve the back-folded Doppler bandwidth in the azimuth pre-processing, azimuth convolution is performed on the wavenumber domain to resolve the back-folded SAR image (space domain) in the azimuth post-processing. In the post azimuth convolution step, only the azimuth component of the signal model is considered for simplicity. Therefore, (34) is rewritten as follows.

$$S_{a0}(\omega_x) = \mathrm{rect}\left[-\frac{\omega_x - b_m x_o}{B_{ins}/A} \right] \cdot \exp[-j\omega_x x_o] \tag{36}$$

The selected azimuth chirp signal to be used for the post azimuth convolution and the result of the convolution are as follows, respectively.

$$S_{c2}(\omega_x) = \exp\left[j\frac{1}{2} \cdot \frac{\omega_x^2}{b_m} \right] \tag{37}$$

$$\begin{aligned} S_{conv}(\omega_x) &= S_{a0}(\omega_x) * S_{c2}(\omega_x) \\ &= S_{c2}(\omega_x) \cdot \int \left(S_{a0}(\omega_u) \cdot S_{c2}(\omega_u) \right) \\ &\quad \times \exp\left[-j\frac{1}{b_m} \omega_x \omega_u \right] d\omega_u \end{aligned} \tag{38}$$

Note that (37) is selected because it removes the dependency of the Doppler band shift on the azimuth spatial location. When the dependency is removed, the phase difference according to the azimuth spatial location of the target does not occur. The big parenthesis term in the integral sign is the first multiplication step in the post azimuth convolution in Fig. 3. The result of multiplying (36) and (37) is as follows.

$$S_{a1}(\omega_x) = \mathrm{rect}\left[-\frac{\omega_x - b_m x_o}{B_{ins}/A} \right] \cdot \exp\left[-j\omega_x x_o + j\frac{1}{2} \cdot \frac{\omega_x^2}{b_m} \right] \tag{39}$$

The next step is to implement the integral in (38), which is very tedious and complicated. But fortunately, it has been proven that the integration process can be replaced by IFFT if the number of azimuth pixels is set to a specific value [36]. It is notable that IFFT is used since convolution is performed in the wavenumber domain. The condition is as follows:

$$N_2 = -\frac{b_m \cdot X_1 \cdot X_{out}}{2\pi} \tag{40}$$

where N_2 is the number of final azimuth pixels and X_{out} is the intentionally extended azimuth extent after reducing the number of azimuth samples. A minus sign is added because b_m is a negative value. Considering the azimuth SWD in Fig. 6, the output azimuth extent must include x_{start} and x_{end} to resolve the back-folded SAR image in the azimuth space domain. Therefore, X_{out} must satisfy the following condition.

$$X_{out} \geq X_{tot} - X_{ss} = AX_{tot} \tag{41}$$

Therefore, N_2 is determined by determining the X_{out} value that satisfies condition (41) and substituting it into (40). Now that the integration process is replaced by IFFT, the following equation is obtained by implementing the azimuth IFFT using the POSP technique.

$$S_{a2}(\omega_x) = \text{rect}\left[-\frac{\omega_x}{B_{ins}/A}\right] \cdot \exp\left[-j\frac{1}{2} \cdot \frac{(\omega_x + b_m x_o)^2}{b_m}\right] \tag{42}$$

The final step of the post azimuth convolution is to perform the multiplication before the integral sign in (38). Multiplying (42) by S_{c2}, the following equation is obtained.

$$S_{a3}(\omega_x) = \text{rect}\left[\frac{\omega_x}{B_{ins}/A}\right] \cdot \exp[-j\omega_x x_o] \tag{43}$$

The rectangular function in (43) means that the Doppler bandwidth of all targets is unified as B_{ins}/A and exists within the baseband regardless of their azimuth spatial locations. The focused final SAR signal model is obtained when the azimuth IFFT (azimuth compression) is performed as the last step of the proposed algorithm.

$$s_{a4}(x) = \text{sinc}\left[\frac{1}{2} \cdot \frac{B_{ins}}{A} \cdot (x - x_o)\right] \tag{44}$$

(44) shows that the target is compressed at its correct azimuth spatial location without any phase errors. The azimuth SWD after the azimuth post-processing is obtained in Fig. 7. The back-folded SAR image is resolved because the azimuth processing extent is extended through the azimuth convolution so that the azimuth processing extent X_{out} includes x_{start} and x_{end}. Note that although the processing Doppler bandwidth is compressed to $B_1 = 2\pi N_2/X_{out} = -b_m \cdot X_1 = B_{ins}/A$ due to the post azimuth convolution, the aliasing does not occur. The final SAR signal model is

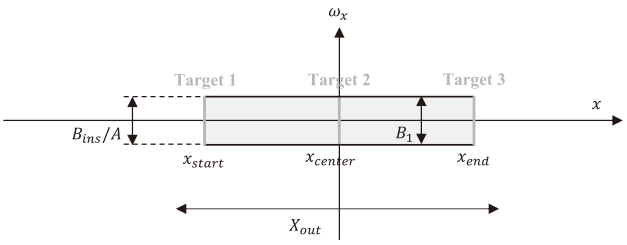

FIGURE 7. Azimuth SWD of sliding mode SAR signal after the post azimuth convolution process.

rewritten as follows in consideration of the complete two-dimensional signal.

$$s_{out}(x, \omega_r) = \text{sinc}\left[\frac{1}{2} \cdot \frac{B_{ins}}{A} \cdot (x - x_o)\right] \times \text{sinc}\left[\frac{R}{2\beta} \cdot (\omega_r - 2b \cdot (r_o - r_c))\right] \tag{45}$$

Contrary to the conventional FSA, the SAR image domain in the azimuth is the space (time) domain. This means that a wide observable scene size is secured in the azimuth direction, and therefore, is suitable for sliding mode data processing. This is proved in Section IV.

IV. RESULTS AND DISCUSSIONS

This Section presents the results of point target simulations and actual SAR raw data processing to verify the validity and practicality of the proposed algorithm. The results are compared with the conventional sub-aperture FSA. A comparison with other sliding spotlight algorithms is also discussed to emphasize the specialty of the proposed method in processing the dechirped sliding mode data. The dechirped data used in the actual SAR raw data experiment is acquired by Thales Alenia's SAR system and are observations of Ayers Rock in Australia in sliding mode. The SAR system specifications and parameters used in the virtual point target simulations and the actual raw SAR data experiments are listed in Table 1.

TABLE 1. Point target simulation parameters.

Parameter	Value
Center frequency	9.66 GHz
System PRF	3612.72 Hz
Pulse bandwidth	212.70 MHz
Bandwidth after dechirp-on-receive	73.38 MHz
Sampling frequency	142.50 MHz
Effective platform velocity	7351.51 m/s
Total azimuth time	3.25 s
Range to scene center	685.70 km
Range to beam rotation center	1203.59 km
Sliding factor	0.43

The locations of the virtual point targets and the designed data acquisition geometry are shown in Fig. 8. The nine targets are r_s apart in the range and x_s apart in the azimuth directions, respectively. To generate the dechirped simulation

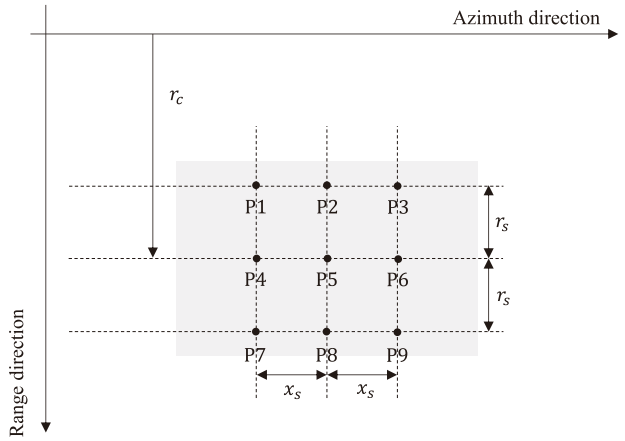

FIGURE 8. Designed imaging area for point target simulations. The squint angle is assumed as zero for convenience.

data, the deramping operation is performed by mixing the expected reflected signal from the targets and the reference signal based on the image scene center [3]. On the other hand, because the conventional sub-aperture FSA in [19] is designed for staring mode data, it is obvious that it has limitations in processing sliding mode data without proper modifications. Therefore, a modified sub-aperture FSA considering the data acquisition geometry of sliding mode [26] is used to meaningfully compare the simulation results with the sub-aperture method.

The point target simulation results of the data for the case where $r_s = 2$km and $x_s = 2$km are given in Fig. 9. Both the proposed and conventional methods compressed all targets at their appropriate positions. To provide a more detailed comparison of the focusing performance, a point target analysis is performed on $P1$, $P5$, and $P9$ targets indicated by white arrows in Fig. 9. The two-dimensional impulse response functions of the targets are shown in Fig. 10 and the SAR quality parameters are listed in Table 2. As shown in Fig. 10(a-c) and Table 2, the proposed method compresses point targets precisely in both range and azimuth directions regardless of range or azimuth displacement of the targets from the SAR image center. In contrast, as shown in Fig. 10(d-f) and Table 2, the azimuth compression performance of the conventional method degrades when there is a significant range displacement of the point targets from the SAR image center.

The reason for the degradation is due to the characteristics of the azimuth compression step of the conventional FSA. In the conventional FSA, the azimuth focusing is performed through a combination of azimuth scaling followed by azimuth deramping operation. Because the azimuth scaling process causes a spatial shift of the signals in the azimuth direction, an azimuth space shift function needs to be introduced to compensate for the shift. The required azimuth space shift is defined as the difference between the center positions of the signal before and after azimuth scaling, as follows [19]:

$$x_v(r_o) = \frac{x_{max}(r_o) + x_{min}(r_o)}{2} - \frac{x_{begin} + x_{fin}}{2} \tag{46}$$

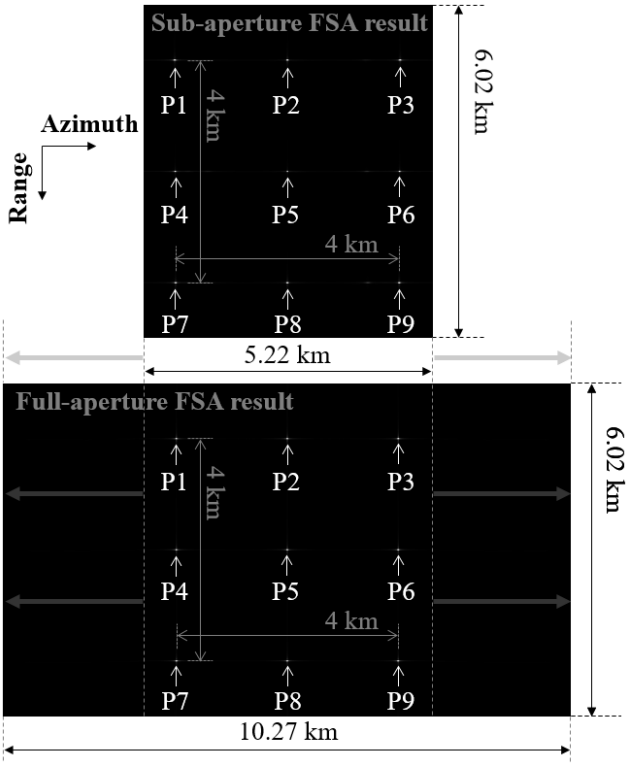

FIGURE 9. Point target simulation results ($r_s = 2$km and $x_s = 2$km). The top and bottom SAR images are the results of the conventional sub-aperture and the proposed full-aperture FSA methods, respectively.

where x_{max} and x_{min} are the maximum and minimum azimuth spatial positions of the signals after azimuth scaling, respectively, and x_{begin} and x_{fin} are the beginning and finishing azimuth locations of the illumination. However, this parameter becomes inaccurate as the range displacement from the center of the SAR image increases because fixed values of x_{begin} and x_{fin} according to r_c are assumed as follows, while they actually depend on r_o [19]:

$$x_{begin} = r_c \cdot \tan(\theta_{begin}) \tag{47}$$

$$x_{fin} = r_c \cdot \tan(\theta_{fin}) \tag{48}$$

where θ_{begin} and θ_{fin} are the squint angles at the beginning and finishing locations. Therefore, as the range displacement increases from the center of the SAR image, the azimuth compression performance deteriorates in the conventional sub-aperture FSA.

On the other hand, because the azimuth compression process of the proposed full-aperture method is replaced with a single modified azimuth-matched filter (33) without the azimuth scaling and the azimuth space shift function, there is no compression performance degradation in the azimuth direction due to range displacement. Additionally, the proposed method has precise azimuth compression performance because it accurately performs RCMC regardless of range displacements by introducing the new scaling factor (28) that depends on r_o. Comparative images in the two-dimensional wavenumber domain before and after performing RCMC in

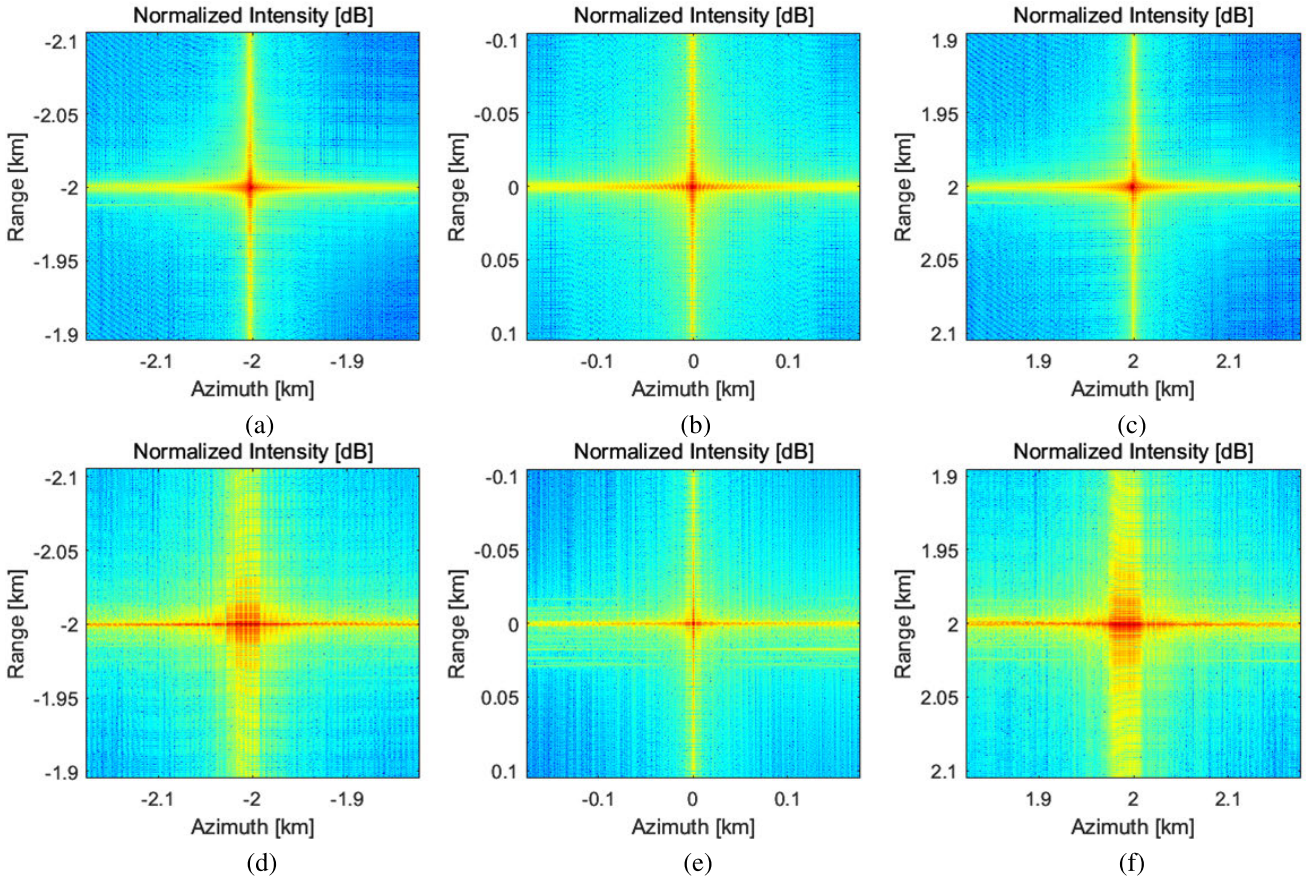

FIGURE 10. Two-dimensional impulse response functions of point targets (a) $P1$ (Proposed), (b) $P5$ (Proposed), (c) $P9$ (Proposed), (d) $P1$ (Conventional), (e) $P5$ (Conventional), (f) $P9$ (Conventional).

TABLE 2. Comparison of SAR quality parameters of simulated point targets.

Method	Proposed full-aperture FSA						Conventional sub-aperture FSA					
Target	Resolution (m)		PSLR (dB)		ISLR (dB)		Resolution (m)		PSLR (dB)		ISLR (dB)	
	Range	Azimuth	Range	Azimuth	Range	Azimuth	Range	Azimuth	Range	Azimuth	Range	Azimuth
$P1$	0.70	0.87	-13.27	-13.26	-10.09	-9.96	0.70	21.36	-13.26	-6.46	-10.07	-5.68
$P5$	0.70	0.87	-13.26	-13.26	-10.05	-10.12	0.70	0.87	-13.27	-13.26	-10.05	-10.02
$P9$	0.70	0.87	-13.27	-13.26	-10.16	-10.07	0.70	21.65	-13.27	-6.60	-9.92	-5.61

the point target simulation are shown in Fig. 11. The proposed method implemented RCMC accurately regardless of range displacements.

In addition, the proposed method is more suitable for sliding mode data processing as it provides a wider observable azimuth extent compared to the conventional method, as confirmed in Fig. 9. To emphasize this property, additional point target simulations for the case where $r_s = 2$km and $x_s = 5$km are performed. As shown in Fig. 12, the proposed method makes all targets show up at their actual locations without aliasing. On the other hand, the sub-aperture method caused azimuth aliasing in the SAR image domain, resulting in targets on the right and left sides appearing at reversed azimuth locations. This is because the conventional sub-aperture FSA has a limited observable azimuth scene size depending on the system PRF value, as the azimuth SAR image domain is the frequency domain. The observable azimuth extents of the proposed full-aperture and conventional sub-aperture FSA are as follows.

$$X_{full} = A \cdot X_{tot} \tag{49}$$

$$X_{sub} = \frac{2\pi}{b_a \cdot \Delta x} = \frac{2\pi}{b_a} \cdot \frac{1}{v_r} \cdot \text{PRF} \tag{50}$$

From the given simulation parameters, the observable azimuth extents for full and sub-aperture methods are about 10.27km and 5.22km, respectively. The 5.22km value coincides with the wrong azimuth locations of the aliased targets $P1, P4, P7 : (0.22 = -5 + 5.22)$km and $P3, P6, P9 : (-0.22 = 5 - 5.22)$km. In order for the sub-aperture method to secure the same level of observable azimuth extent as the full-aperture approach, the system PRF must be doubled,

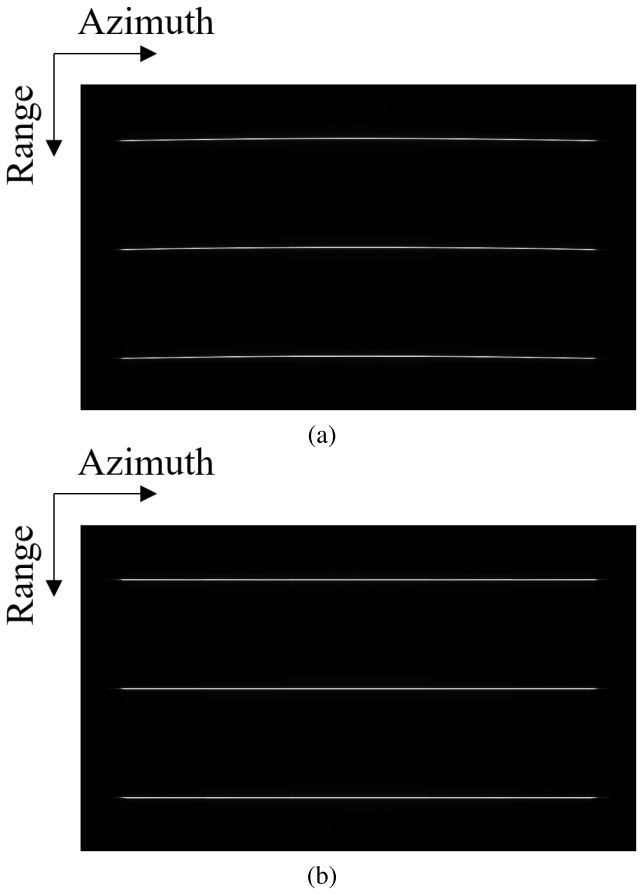

FIGURE 11. Two-dimensional wavenumber domain signal (a) before performing RCMC, (b) after performing RCMC.

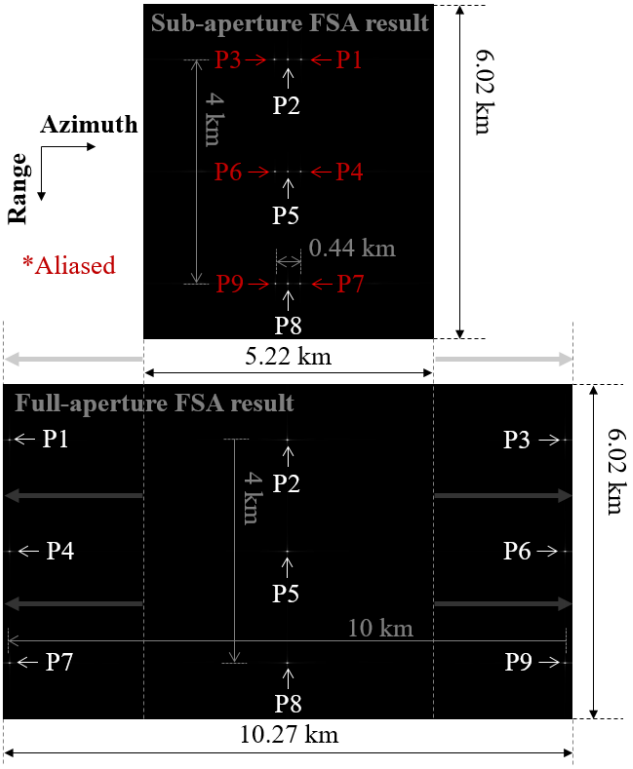

FIGURE 12. Point target simulation results (r_s = 2km and x_s = 5km). The top and bottom SAR images are the results of the conventional sub-aperture and the proposed full-aperture FSA methods, respectively. Note that P1, P3, P4, P6, P7, and P9 are aliased in the SAR image of the sub-aperture method.

TABLE 3. Comparison between the proposed and various other methods for sliding mode.

Method	Approach	Compatible signal model
Modified [19]	Sub-aperture	**Dechirped**
[20 – 26]	Sub-aperture	Chirped
[27 – 36]	**Full-aperture**	Chirped
Proposed	**Full-aperture**	**Dechirped**

which means that an enormous amount of zero-padding is required and may cause severe range ambiguity.

The validity of the proposed algorithm is quantitatively verified through the point target simulations. The proposed full-aperture method has precise focusing performance in both range and azimuth for a wide image swath.

To verify the practicality of the proposed algorithm, actual SAR raw data processing is performed. The satellite photograph of the target area and SAR image results of the proposed full-aperture and the conventional sub-aperture FSA methods are given in Fig. 13. Both the proposed and conventional methods provide focused SAR images that match the satellite photograph. For a more precise comparison, SAR images of the area indicated by the red box in Fig. 13(a) are enlarged in Fig. 14. It is noteworthy that the SAR image of the sub-aperture method is slightly out of focus compared to that of the proposed method since the observed region has a significant range displacement from the center of the SAR image. This result is consistent with the point target simulation results in which the focusing performance of the conventional FSA in the azimuth direction deteriorates when the range displacements of the point target from the center of the SAR image are large. The practicality of the proposed algorithm is demonstrated through the fact that the SAR images processed with actual raw data matched the satellite photograph.

In addition, Table 3 is given to compare the compatible signal models of the proposed and other sliding SAR processing algorithms. As shown in Table 3, many sub- and full-aperture methods have been developed to process sliding mode data. However, most methods [20], [21], [22], [23], [24], [25], [26], [27], [28], [29], [30], [31], [32], [33], [34], [35], [36] focus on processing chirped signal models, and these techniques have limitations in processing the dechirped signal models. This is because the dechirped and the chirped signal model have a significant difference, such as the presence or absence of RVP, and therefore, precise SAR images are not generated unless the algorithms are significantly modified according to the signal model.

The conventional sub-aperture FSA in [19] developed frequency scaling, a powerful method to process the dechirped

FIGURE 13. Images of Ayers Rock. The range and azimuth swaths of the image are about 5.55*km* and 4.42*km*, respectively. (a) satellite photograph, (b) proposed full-aperture FSA, (c) conventional sub-aperture FSA.

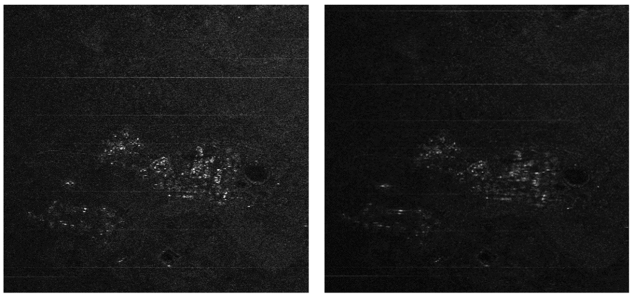

FIGURE 14. Enlarged SAR images (a) Proposed method, (b) conventional method.

signal. However, since the algorithm is designed for the staring mode, frequency aliasing may occur, or focusing will not be performed properly when applied directly to the sliding mode data. Therefore, the modified version of [19] for the sliding mode was selected as a subject of the comparison with the proposed full-aperture method. However, the method showed a focusing performance degradation phenomenon in the azimuth direction when there is a significant range displacement from the center of the SAR image. In addition, the observable azimuth extent is limited by the PRF value, which means the sub-aperture FSA is unsuitable for processing sliding mode data because the sliding mode acquires signals corresponding to a relatively wide azimuth extent. On the other hand, the proposed full-aperture FSA showed consistent focusing performance in both range and azimuth over a wide area. And also, a wide azimuth extent was secured, which means the method is suitable for sliding mode data processing.

V. CONCLUSION

In this paper, a complete signal model and a full-aperture processing algorithm for the dechirped sliding mode data have been proposed. We incorporated the FSA, which is a powerful algorithm to process the dechirped signal, into the full-aperture method. By analyzing the modifications in the signal model according to azimuth preliminary convolution and Fourier transforms, a new signal model of the azimuth convoluted sliding mode data with the dechirp-on-receive is presented in the range-Doppler domain. Based on the signal model, a modified scaling factor for sliding mode and full-aperture method is introduced. And also, the azimuth compression parts required in the conventional FSA have been replaced with a single multiplication process with the modified azimuth-matched filter, which makes the algorithm simple and accurate. To verify the validity of the proposed algorithm, point target simulations for two scene sizes are performed. The proposed full-aperture FSA method is advantageous in that it provides precise and consistent compression performance over a wide scene size in both range and azimuth compared to the sub-aperture one. In addition, we demonstrated that the proposed method is more suitable for processing sliding mode data than the sub-aperture method by showing that a wide observable azimuth extent is obtained. The practicality of the algorithm is further demonstrated by processing actual raw data and providing a proper SAR image that matches the satellite photograph. It was discussed that the proposed algorithm has the advantage of being able to process dechirp-on-receive data compared to other sliding SAR algorithms. We expect the proposed algorithm to be a good reference for designing a processor for the dechirped sliding mode data.

Note that the conventional hyperbolic range equation model from the straight path is not suitable for ultrahigh-resolution SAR image generation when obtaining raw data from long synthetic apertures in curved orbits, such as spaceborne sliding mode. In this case, an accurate range model considering the curved orbital effect is required, and the algorithm should be modified accordingly.

Future work includes detailed quantitative comparisons between the proposed and other sliding mode processing algorithms. This requires modifying the existing algorithms to be compatible with the dechirped signal model.

REFERENCES

[1] I. G. Cumming and F. H. Wong, *Digital Processing of Synthetic Aperture Radar Data: Algorithms and Implementation*. London, U.K.: Artech House Inc., 2005.

[2] C.-K. Kim, J.-S. Lee, J.-S. Chae, and S.-O. Park, "A modified stripmap SAR processing for vector velocity compensation using the cross-correlation estimation method," *J. Electromagn. Eng. Sci.*, vol. 19, no. 3, pp. 159–165, Jul. 2019.

[3] W. G. Carrara, R. S. Goodman, and R. M. Majewski, *Spotlight Synthetic Aperture Radar: Signal Processing Algorithms*. Norwood, MA, USA: Artech House Inc., 1995.

[4] R. Yang, H. Li, S. Li, P. Zhang, L. Tan, X. Gao, and X. Kang, *High-Resolution Microwave Imaging*. Singapore: National Defense, 2018.

[5] M. P. Nguyen, "Omega-K algorithm—A generalization for highly squinted spotlight SAR imaging with dechirp-on-receive," in *Proc. 3rd Int. Asia–Pacific Conf. Synth. Aperture Radar (APSAR)*, Sep. 2011, pp. 1–4.

[6] Z. Mo, R. Li, J. Yang, C. Liu, and W. Li, "A photonic dechirp-on-receive pulse synthetic aperture radar using a phase correlated optical reference signal in a DSP-based optical coherent receiver," *IEEE Access*, vol. 9, pp. 164903–164911, 2021.

[7] D. Zhu, "A novel approach to residual video phase removal in spotlight SAR image formation," in *Proc. IET Int. Conf. Radar Syst.*, 2007, pp. 1–4.

[8] D. Zhu, M. Shen, and Z. Zhu, "Some aspects of improving the frequency scaling algorithm for dechirped SAR data processing," *IEEE Trans. Geosci. Remote Sens.*, vol. 46, no. 6, pp. 1579–1588, Jun. 2008.

[9] D. P. Belcher and C. J. Baker, "Hybrid strip-map/spotlight SAR," in *Proc. IEE Colloq. Radar Microw. Imag.*, London, U.K., Mar. 1994, pp. 2-1–2-7.

[10] D. P. Belcher and C. J. Baker, "High resolution processing of hybrid strip-map/spotlight mode SAR," *IEE Proc. Radar, Sonar Navigat.*, vol. 143, no. 6, pp. 366–374, Dec. 1996.

[11] S. Henrion, L. Savy, and J.-G. Planes, "Properties of hybrid strip-map/spotlight spaceborne SAR processing," in *Proc. IEEE Int. Geosci. Remote Sens. Symp.*, Hamburg, Germany, Feb. 1999, pp. 530–534.

[12] A. Moreira and R. Spielbauer, "Combining a subaperture and chirp scaling approach for real-time SAR processing," *Int. J. Electron. Commum.*, vol. 5, no. 2, pp. 139–144, 1996.

[13] A. Moreira, "Real-time synthetic aperture radar (SAR) processing with a new subaperture approach," *IEEE Trans. Geosci. Remote Sens.*, vol. 30, no. 4, pp. 714–722, Jul. 1992.

[14] G.-C. Sun, Y. Liu, M. Xing, S. Wang, J. Yang, Z. Bao, and M. Bao, "A real-time unified focusing algorithm (RT-UFA) for multi-mode SAR via azimuth sub-aperture complex-valued image combining and scaling," *IEEE Trans. Geosci. Remote Sens.*, vol. 60, 2022, Art. no. 5212117.

[15] F. Zhou, J. Yang, G. Sun, and J. Zhang, "A real-time imaging processing method based on modified RMA with sub-aperture images fusion for spaceborne spotlight SAR," in *Proc. IEEE Int. Geosci. Remote Sens. Symp.*, Waikoloa, HI, USA, Sep. 2020, pp. 1905–1908.

[16] G.-C. Sun, Y. Liu, M. Xing, S. Wang, L. Guo, and J. Yang, "A real-time imaging algorithm based on sub-aperture CS-dechirp for GF3-SAR data," *Sensors*, vol. 18, no. 8, p. 2562, Aug. 2018.

[17] Z. Li, Y. Liang, M. Xing, and J. Wu, "A sub-aperture imaging algorithm for highly squinted SAR based on frequency phase correction," in *Proc. IEEE 5th Asia–Pacific Conf. Synth. Aperture Radar (APSAR)*, Singapore, Sep. 2015, pp. 254–257.

[18] A. Moreira, J. Mittermayer, and R. Scheiber, "Extended chirp scaling algorithm for air- and spaceborne SAR data processing in stripmap and ScanSAR imaging modes," *IEEE Trans. Geosci. Remote Sens.*, vol. 34, no. 5, pp. 1123–1136, Sep. 1996.

[19] J. Mittermayer, A. Moreira, and O. Loffeld, "Spotlight SAR data processing using the frequency scaling algorithm," *IEEE Trans. Geosci. Remote Sens.*, vol. 37, no. 5, pp. 2198–2214, Sep. 1999.

[20] Y. Wu, G.-C. Sun, C. Yang, J. Yang, M. Xing, and Z. Bao, "Processing of very high resolution spaceborne sliding spotlight SAR data using velocity scaling," *IEEE Trans. Geosci. Remote Sens.*, vol. 54, no. 3, pp. 1505–1518, Mar. 2016.

[21] F. He, Q. Chen, Z. Dong, and Z. Sun, "Processing of ultrahigh-resolution spaceborne sliding spotlight SAR data on curved orbit," *IEEE Trans. Aerosp. Electron. Syst.*, vol. 49, no. 2, pp. 819–839, Apr. 2013.

[22] P. Prats, R. Scheiber, J. Mittermayer, A. Meta, and A. Moreira, "Processing of sliding spotlight and Tops SAR data using baseband azimuth scaling," *IEEE Trans. Geosci. Remote Sens.*, vol. 48, no. 2, pp. 770–780, Feb. 2010.

[23] M. Yang, F. Kong, D. Zhu, and X. Yu, "Sliding spotlight SAR data focusing based on subaperture with line-of-sight motion compensation," in *Proc. IEEE Int. Geosci. Remote Sens. Symp. (IGARSS)*, Fort Worth, TX, USA, Jul. 2017, pp. 1645–1648.

[24] Y. Guo, L. Cui, P. Wang, and J. Chen, "A modified imaging algorithm for space-borne sliding spotlight SAR based on azimuth non-uniform sampling," in *Proc. IEEE Int. Geosci. Remote Sens. Symp.*, Kuala Lumpur, Malaysia, Jul. 2022, pp. 1820–1823.

[25] H. Kuang, Z. Wang, Z. Lu, Y. Zhu, Y. Liu, and M. Xu, "An improved imaging algorithm for high resolution spaceborne squinted sliding spotlight SAR," in *Proc. 6th Asia–Pacific Conf. Synth. Aperture Radar (APSAR)*, Xiamen, China, Nov. 2019, pp. 1–4.

[26] J. Mittermayer, R. Lord, and E. Borner, "Sliding spotlight SAR processing for TerraSAR-X using a new formulation of the extended chirp scaling algorithm," in *Proc. IEEE Int. Geosci. Remote Sens. Symp.*, Toulouse, France, May 2003, pp. 1462–1464.

[27] Q. Zhang, F. Xiao, Z. Ding, M. Ke, and T. Zeng, "Sliding spotlight mode imaging with GF-3 spaceborne SAR sensor," *Sensors*, vol. 18, no. 2, p. 43, Dec. 2017.

[28] H. Fan, L. Zhang, Z. Zhang, W. Yu, and Y. Deng, "On the processing of Gaofen-3 spaceborne dual-channel sliding spotlight SAR data," *IEEE Trans. Geosci. Remote Sens.*, vol. 60, 2022, Art. no. 5202912.

[29] T. Fang, Y. Deng, D. Liang, L. Zhang, H. Zhang, H. Fan, and W. Yu, "Multichannel sliding spotlight SAR imaging: First result of GF-3 satellite," *IEEE Trans. Geosci. Remote Sens.*, vol. 60, 2022, Art. no. 5204716.

[30] Y. Wang, S. Zhang, and Y. Jia, "Processing azimuth-time domain aliasing in spaceborne sliding-spotlight SAR imaging," in *Proc. 14th Eur. Conf. Antennas Propag. (EuCAP)*, Copenhagen, Denmark, Mar. 2020, pp. 1–5.

[31] G.-C. Sun, Y. Wu, J. Yang, M. Xing, and Z. Bao, "Full-aperture focusing of very high resolution spaceborne-squinted sliding spotlight SAR data," *IEEE Trans. Geosci. Remote Sens.*, vol. 55, no. 6, pp. 3309–3321, Jun. 2017.

[32] F. He, Z. Dong, Y. Zhang, G. Jin, and A. Yu, "Processing of spaceborne squinted sliding spotlight and HRWS Tops mode data using 2-D baseband azimuth scaling," *IEEE Trans. Geosci. Remote Sens.*, vol. 58, no. 2, pp. 938–955, Feb. 2020.

[33] G. Franceschetti, R. Guida, A. Iodice, D. Riccio, and G. Ruello, "Efficient simulation of hybrid stripmap/spotlight SAR raw signals from extended scenes," *IEEE Trans. Geosci. Remote Sens.*, vol. 42, no. 11, pp. 2385–2396, Nov. 2004.

[34] J. Chen, H. Kuang, W. Yang, W. Liu, and P. Wang, "A novel imaging algorithm for focusing high-resolution spaceborne SAR data in squinted sliding-spotlight mode," *IEEE Geosci. Remote Sens. Lett.*, vol. 13, no. 10, pp. 1577–1581, Oct. 2016.

[35] G. Sun, M. Xing, Y. Wang, Y. Wu, Y. Wu, and Z. Bao, "Sliding spotlight and Tops SAR data processing without subaperture," *IEEE Geosci. Remote Sens. Lett.*, vol. 8, no. 6, pp. 1036–1040, Nov. 2011.

[36] W. Xu, Y. Deng, P. Huang, and R. Wang, "Full-aperture SAR data focusing in the spaceborne squinted sliding-spotlight mode," *IEEE Trans. Geosci. Remote Sens.*, vol. 52, no. 8, pp. 4596–4607, Aug. 2014.

[37] R. Lanari, M. Tesauro, E. Sansosti, and G. Fornaro, "Spotlight SAR data focusing based on a two-step processing approach," *IEEE Trans. Geosci. Remote Sens.*, vol. 39, no. 9, pp. 1993–2004, Sep. 2001.
[38] D. An, X. Huang, T. Jin, and Z. Zhou, "Extended two-step focusing approach for squinted spotlight SAR imaging," *IEEE Trans. Geosci. Remote Sens.*, vol. 50, no. 7, pp. 2889–2900, Jul. 2012.
[39] D. Zhu, T. Xiang, W. Wei, Z. Ren, M. Yang, Y. Zhang, and Z. Zhu, "An extended two step approach to high-resolution airborne and spaceborne SAR full-aperture processing," *IEEE Trans. Geosci. Remote Sens.*, vol. 59, no. 10, pp. 8382–8397, Oct. 2021.
[40] W. Xu, P. Huang, Y. Deng, J. Sun, and X. Shang, "An efficient approach with scaling factors for TOPS-mode SAR data focusing," *IEEE Geosci. Remote Sens. Lett.*, vol. 8, no. 5, pp. 929–933, Sep. 2011.
[41] R. K. Raney, H. Runge, R. Bamler, I. G. Cumming, and F. H. Wong, "Precision SAR processing using chirp scaling," *IEEE Trans. Geosci. Remote Sens.*, vol. 32, no. 4, pp. 786–799, Jul. 1994.
[42] M. Ren, H. Zhang, W. Yu, Z. Chen, and H. Li, "An efficient full-aperture approach for airborne spotlight SAR data processing based on time-domain dealiasing," *IEEE J. Sel. Topics Appl. Earth Observ. Remote Sens.*, vol. 15, pp. 2463–2475, 2022.
[43] D. Li, T. Shi, Y. Bao, Y. Mo, and X. Mao, "Modified full-aperture omega-k algorithm for circular-track ringmap mode SAR," in *Proc. 6th Asia–Pacific Conf. Synth. Aperture Radar (APSAR)*, Xiamen, China, Nov. 2019, pp. 1–6.
[44] S. Zhang, G. Sun, and M. Xing, "Full aperture imaging algorithm for highly squinted TOPS SAR," *J. Syst. Eng. Electron.*, vol. 27, no. 6, pp. 1168–1175, Dec. 2016.
[45] R. K. Raney, "A new and fundamental Fourier transform pair," in *Proc. Int. Geosci. Remote Sens. Symp.*, Houston, TX, USA, 1992, pp. 106–107.
[46] A. Papoulis, *Systems and Transforms With Applications in Optics*. New York, NY, USA: McGraw-Hill, 1968.
[47] G. W. Davidson and I. Cumming, "Signal properties of spaceborne squint-mode SAR," *IEEE Trans. Geosci. Remote Sens.*, vol. 35, no. 3, pp. 611–617, May 1997.

YOUNG-GEUN KANG was born in Daejeon, South Korea, in February 1994. He received the B.S. degree in electrical and electronic engineering from Yonsei University, Seoul, South Korea, in 2018, and the M.S. degree in electrical engineering from the Korea Advanced Institute of Science and Technology (KAIST), Daejeon, in 2020, where he is currently pursuing the Ph.D. degree in electrical engineering.

His research interests include synthetic aperture radar (SAR), radar systems, and radar data processing.

SEONG-OOK PARK (Senior Member, IEEE) was born in Kyungpook, South Korea, in December 1964. He received the B.S. degree in electrical engineering from Kyungpook National University, Kyungpook, in 1987, the M.S. degree in electrical engineering from the Korea Advanced Institute of Science and Technology (KAIST), Daejeon, South Korea, in 1989, and the Ph.D. degree in electrical engineering from Arizona State University, Tempe, AZ, USA, in 1997.

From March 1989 to August 1993, he was a Research Engineer at Korea Telecom, Daejeon, working with microwave systems and networks. He joined the Telecommunication Research Center, Arizona State University, until September 1997. Since October 1997, he has been a Professor with KAIST. His research interests include mobile handset antennas, radar systems, and analytical and numerical techniques in the field of electromagnetics.

Dr. Park is a member of Phi Kappa Phi.